Received: 27 June 2026 | Revised:04 August 2026 | Accepted: 18 August 2026

https://doi.org/10.56946/jce.v5i2.948
Volume 5 (2): 17-28

Journal of Chemistry and Environment

Research Article

Alkyne-Linked Spirobifluorene D–π–A–π–D Emitters: Synthesis, Solution-State ICT Photophysics, and Comparative Acceptor Effects

Maria Siddique[1], Mazhar Khan[1*], Muhammad Mubashir Khan[2], Amir Zeeshan[3], Rafaqat Khan[4], Zeeshan Akmal[1], Muhammad Sohail Tahir[5], and Qifan Yan[1*]

[1]Key Laboratory for Advanced Materials and Feringa Nobel Prize Scientist Joint Research Center, School of Chemistry and Molecular Engineering, East China University of Science & Technology, Shanghai 200237, P. R. China.
[2]Department of Physics, University of Agriculture, Faisalabad, 38000, Pakistan.
[3]School of Science, Harbin Institute of Technology, Campus of University Town of Shenzhen, Shenzhen 518005, P. C. China.
[4]Institute of Functional Porous Materials, School of Materials Science and Engineering, Zhejiang Sci-Tech University, Hangzhou 310018, China.
[5]University of Science and Technology of China.

*Correspondence: Mazhar Khan (mazharkhan57@yahoo.com); Qifan Yan (yanqifan@ecust.edu.cn)

Abstract

The construction of sterically demanding donor-acceptor architectures remains a significant challenge in organic materials chemistry. Herein, two D-π-A-π-D type compounds, BTD-DPA and QXN-DPA, incorporating a 9,9′-spirobifluorene core with benzothiadiazole and quinoxaline acceptor units, were synthesized and investigated in solution. Conventional cross-coupling approaches, including Stille and Negishi reactions, were unsuccessful because of severe steric congestion between donor-bridge fragments and acceptor units. Introduction of alkyne spacers through Sonogashira coupling successfully enabled access to the target structures. Both compounds exhibited good stability in aerated chloroform solution, with no observable degradation after 30 days as monitored by ^{1}H NMR spectroscopy. Photophysical studies revealed absorption maxima at 352 nm for BTD-DPA and 310 nm for QXN-DPA, with corresponding emission maxima at 400 nm and 450 nm, respectively. Fluorescence quantum yields of 16.4% for BTD-DPA and 14.3% for QXN-DPA were measured in toluene. Solvent-dependent fluorescence behavior indicated the presence of intramolecular charge-transfer excited states. Computational analysis further supported the mixed localized π-π* and charge-transfer character of the electronic excitations. Comparative analysis demonstrated that acceptor identity significantly influences the absorption energy, emission wavelength, and fluorescence efficiency of these spirobifluorene-based systems. These findings provide insight into structure-property relationships in sterically hindered donor–acceptor luminophores and establish an effective synthetic strategy for their preparation.

Keywords: Spirobifluorene, Benzothiadiazole, Quinoxaline, Donor-acceptora Systems, Sonogashira Coupling

1. Introduction

Donor-acceptor (D-A) organic luminophores have attracted considerable interest because their electronic and optical properties can be effectively tuned through molecular design [1-4]. In such systems, intramolecular charge transfer (ICT) between electron-donating and electron-accepting fragments often gives rise to solvent-dependent emission behavior, tunable fluorescence, and modified excited-state characteristics. The incorporation of π-conjugated bridges between donor and acceptor units further influences electronic communication and photophysical response [4-8]. Spirobifluorene derivatives represent attractive structural platforms for luminescent materials because of their rigid three-dimensional geometry, high thermal stability, and suppression of intermolecular π–π stacking interactions. Their orthogonal arrangement can reduce aggregation-induced quenching while maintaining good solubility and morphological stability. Previous studies have employed spirobifluorene frameworks in D-A molecular systems for investigating charge-transfer photophysics and luminescent behavior [9-15]. Beyond molecular luminophores, recent photocatalytic studies based on S-scheme heterostructures, redox-site engineering, single-atom sites, MXene composites, and MOF-based photocatalysts further demonstrate that controlled electronic communication and spatial charge separation are central principles for designing photoactive materials.

Among electron-accepting building blocks, benzothiadiazole (BTD) and quinoxaline (QXN) are widely utilized because of their electron-deficient aromatic structures and strong influence on excited-state electronic properties. Benzothiadiazole generally exhibits stronger electron-withdrawing character, whereas quinoxaline provides extended conjugation and tunable electronic delocalization. However, direct comparisons of these acceptors within structurally consistent spirobifluorene-based D-π-A-π-D systems remain relatively limited [16-20]. In addition to

electronic considerations, the synthesis of sterically hindered donor–acceptor architectures present substantial challenges. Conventional cross-coupling methods may fail because of steric congestion between bulky donor and acceptor fragments, requiring alternative synthetic strategies for successful molecular construction [21-25].

In this work, two spirobifluorene-centered D-π-A-π-D compounds containing BTD and QXN acceptor units were synthesized through a Sonogashira coupling strategy incorporating alkyne spacers. Their solution-state stability, absorption and emission behavior, solvatochromic properties, and computational electronic structures were investigated. By maintaining identical donor and bridge units while varying the acceptor fragment, this study provides comparative insight into how acceptor identity influences the photophysical behavior of spirobifluorene-based D-A systems. The novelty of this work lies in the introduction of alkyne spacers to overcome the steric limitations that prevented direct Stille and Negishi coupling. Moreover, the use of identical donor and π-bridge units enables a controlled comparison of the effects of BTD and QXN acceptors on the solution-state photophysical properties of the resulting D-π-A-π-D emitters.

2. Materials and Methods

2.1. Experimental instruments

The NMR characterization instrument is Bruker-400 (400 MHz) or Bruker-600 (600 MHz), and the deuterated reagent used is deuterated chloroform ($CDCl_3$) or deuterated DMSO (DMSO-d6). ^1H NMR and ^{13}C NMR both use solvent residual peaks in deuterated chloroform or deuterated DMSO. ^1H NMR and ^{13}C NMR both use the solvent residual peak ($CHCl_3$: 7.26 ppm or DMSO-d6: 2.50 ppm) and the deuterated solvent peak ($CDCl_3$: 77.0 ppm) in deuterated chloroform or deuterated DMSO as the calibration reference peak; The high-resolution mass spectrometry instruments are Waters-GCT mass spectrometer (70 eV electron pulse) and AB Sciex 4800 Plus MALDI-TOF-MS analyzer (HABA as reference model).

2.2. Experimental reagents and pretreatment

All purchased chemicals were used directly without purification or treatment unless otherwise stated. All reactions involving water and oxygen sensitivity were performed using Schlenk bottles under nitrogen protection. The solvents involved in the water-oxygen sensitive reaction are toluene, tetrahydrofuran, diethyl ether, triethylamine, diisopropylamine, and N, N' dimethylformamide (DMF). Among them, tetrahydrofuran and DMF are commercially available with water contents ≤ 50 ppm. For ultra-dry solvents, toluene, triethylamine, and diisopropylamine are redistilled to remove water using calcium hydride (CaH_2). Diethyl ether is redistilled to remove water using metallic sodium. All water-removing solvents are stored in 4A containing high temperature activation. Store the molecular sieve solution in a bottle for later use.

3. Results and discussion

3.1. Synthesis and Structural Characterization

The construction of D-π-A-π-D type compounds bearing benzothiadiazole and quinoxaline acceptors required a carefully designed synthetic sequence to address steric challenges. Our approach began with the preparation of halogented spirobifluorene precursors at both 2,2'- and 3,3'-positions (Figure 1). 9,9'-Spirobifluorene served as the starting material. Nitration followed by amination yielded 2,2'-diaminospirobifluorene (Table S1). The nitration step required optimization: addition of two equivalents of concentrated nitric acid in one portion produced mixtures containing mono- and trinitrated byproducts alongside unreacted starting material, as evidenced by four spots on TLC [26-28]. To address this, batchwise addition of nitric acid was employed. Each portion was added while monitoring by TLC until the starting material and mononitrated product spots nearly disappeared, and the trinitrated product spot just began to appear. The reaction was then stopped, maximizing the yield of the desired dinitrated product. Diazotization followed by iodination with potassium iodide converted the diamine to 2,2'-diiodospirobifluorene. For the 3,3'-substituted analogue, spirobifluorene underwent bromination with N-bromosuccinimide (NBS), followed by diazotization and deamination under hypophosphorous acid conditions to yield 3,3'-dibromospirobifluorene [29-33].

In the diazotization and subsequent iodination of 2,2'-diaminospirobifluorene, initial attempts followed literature conditions using concentrated hydrochloric acid, deionized water, and acetonitrile as solvents. Diazotization and iodination were carried out in an ice-water bath, followed by heating at reflux (90 °C) for 2 h. However, the desired diiodo product could not be obtained. Adjusting the addition order and temperature of the saturated potassium iodide solution also failed to yield the target compound [34-38]. NMR characterization revealed the product to be monoiodospirobifluorene. This was attributed to the high reflux temperature, causing loss of one iodine atom with replacement by hydrogen. Therefore, the reaction was modified: only concentrated hydrochloric acid and deionized water were used as solvents, diazotization and iodination were conducted in an ice-water bath, and the mixture was then stirred at room temperature for 16 h [39]. This successfully yielded 2,2'-diiodospirobifluorene. The addition of copper(I) iodide as a catalyst did not improve the yield. With the halogenated spirobifluorene in hand, Buchwald-Hartwig coupling was employed to connect the diphenylamine donor (Table S2) (Figure 2).

In the diazotization and subsequent iodination of 2,2'-diaminospirobifluorene, initial attempts followed literature conditions using concentrated hydrochloric acid, deionized water, and acetonitrile as solvents. Diazotization and iodination were carried out in an ice-water bath, followed by heating at reflux (90 °C) for 2 h. However, the desired diiodo product could not be obtained.

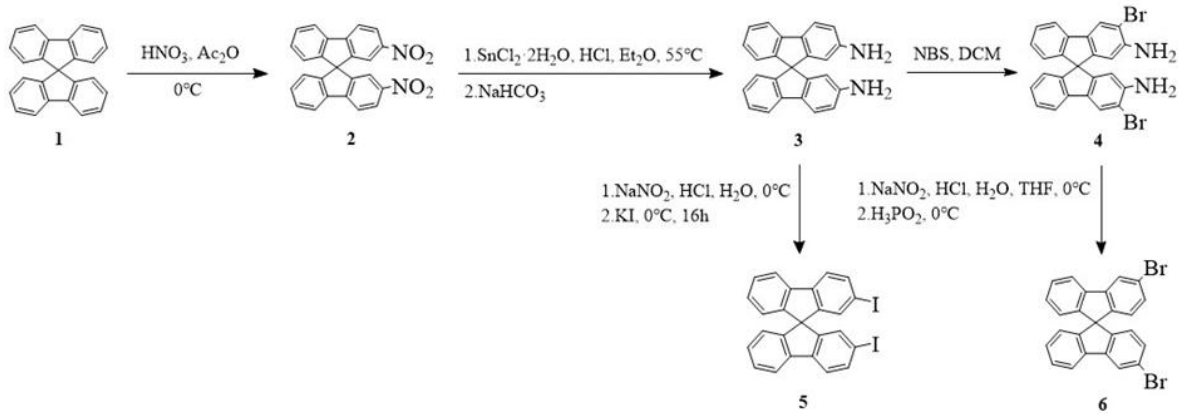

Figure 1. Synthesis of 2,2' and 3,3' halogenated spirobifluorene.

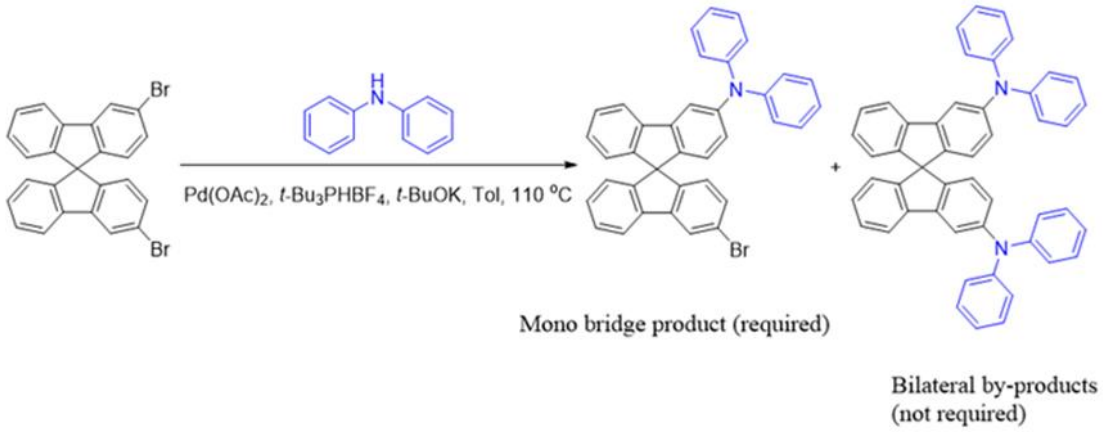

Figure 2. Synthesis of unilateral donor substitution products.

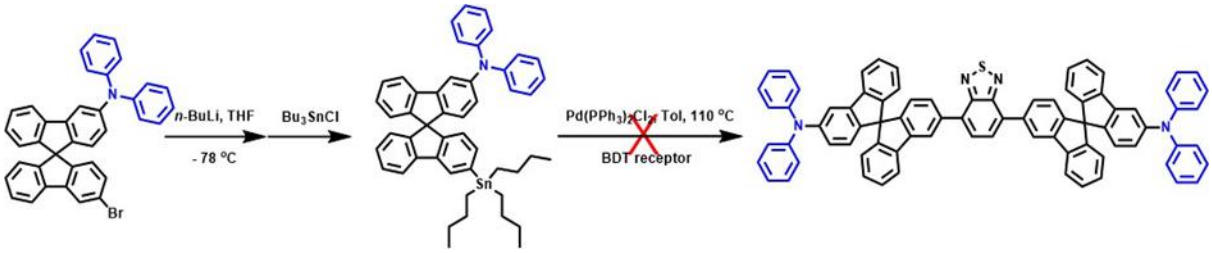

Figure 3. Synthesis of D-π-A luminescent materials (Stille Coupling).

Adjusting the addition order and temperature of the saturated potassium iodide solution also failed to yield the target compound [34-38]. NMR characterization revealed the product to be monoiodospirobifluorene. This was attributed to the high reflux temperature, causing loss of one iodine atom with replacement by hydrogen. Therefore, the reaction was modified: only concentrated hydrochloric acid and deionized water were used as solvents, diazotization and iodination were conducted in an ice-water bath, and the mixture was then stirred at room temperature for 16 h [39]. This successfully yielded 2,2'-diiodospirobifluorene. The addition of copper(I) iodide as a catalyst did not improve the yield. With the halogenated spirobifluorene in hand, Buchwald-Hartwig coupling was employed to connect the diphenylamine donor (Table S3) (Figure 2).

Due to the one-pot preparation, significant quantities of bilaterally substituted byproducts were generated. To increase the yield of the desired unilaterally substituted product, diphenylamine was pre-dissolved in toluene and added dropwise to the reaction solution under nitrogen using a peristaltic pump. During the addition, the reaction mixture turned black. Subsequent TLC monitoring showed that neither unilateral nor bilateral products were formed. This failure was attributed to the peristaltic pump setup compromising the system's airtightness, allowing oxygen ingress and causing the palladium catalyst to form inactive palladium black. The

monosubstituted product was isolated and its structure confirmed by ^{1}H and ^{13}C NMR spectroscopy (Figure S1).

Initial attempts to directly connect donor and acceptor fragments through Stille (Figure 3) and Negishi (Figure 4) coupling reactions were unsuccessful. Various catalyst systems, halogen substitutions, and reaction conditions were examined; however, the desired coupling products could not be isolated. These failures were attributed primarily to severe steric congestion between the substituted spirobifluorene donor fragment and the acceptor units. To overcome this limitation, the molecular design was modified to incorporate alkyne spacers, thereby reducing steric hindrance and facilitating subsequent Sonogashira coupling reactions.

The catalyst and ligand system was then modified, using Pd_2 $(dba)_3$ with the sterically hindered and electron-rich ligand $P(o\text{-}Tol)_3$. Despite these changes, no coupling product was obtained. TLC analysis revealed numerous fluorescent spots not corresponding to the halogenated acceptor, suggesting extensive side reactions of the acceptor under the reaction conditions. These experiments demonstrated that Stille coupling (Table S4) was ineffective for connecting the donor and acceptor in this system. The formation of the donor intermediate was confirmed by ^{1}H and ^{13}C NMR spectroscopy, with spectra provided in the Supporting Information (Figure S2). Negishi coupling was subsequently explored as an alternative method (Figure 4). The donor was treated with n-butyllithium for dehalogenation, followed by the addition of $ZnCl_2$ in tetrahydrofuran to prepare the organozinc reagent. Without isolation, Negishi coupling was performed directly using $Pd(PPh_3)_2$ Cl_2 as a catalyst. However, no product was obtained. The failure of both Stille and Negishi couplings suggested that excessive steric hindrance between the donor and acceptor units prevented bond formation. Therefore, the target structure was modified to incorporate an alkyne linkage between the donor and acceptor, reducing steric congestion and increasing the likelihood of successful coupling [40].

Sonogashira coupling was employed to connect the monosubstituted halogenated spirobifluorene to trimethylsilylacetylene (Figure S2 and Table S5). Initial attempts with the 3,3′-brominated monosubstituted spirobifluorene in a mixed solvent of diisopropylamine and tetrahydrofuran at 60 °C for 12 h yielded no product (Table S4). Increasing the temperature to 80 °C for 12 hours also showed no reaction, with TLC monitoring revealing only starting material. The solvent system was then modified to pure diisopropylamine. Under these conditions, reaction at 60 °C for 12 hours successfully produced the desired TMS-protected acetylene derivative. Optimization of base and temperature revealed that using pure diisopropylamine as solvent at 80 °C for 12 hours provided the highest yield. In contrast, the 2,2'-iodinated monosubstituted spirobifluorene underwent smooth Sonogashira coupling under milder conditions. Reaction in a mixed solvent of diisopropylamine and tetrahydrofuran at room temperature for 12 hours afforded the corresponding product in 90% yield. This marked difference in reactivity highlights the influence of both halogen identity and substitution pattern on coupling efficiency [41, 42]. The structures of compounds A and B were confirmed by ^{1}H and ^{13}C NMR spectroscopy, with spectra provided in the Supporting Information (Figure S3-S4) [10, 21].

The donor-TMS-acetylene compound was then subjected to deprotection of the TMS protecting group using K_2CO_3 in a mixed solvent of dichloromethane and methanol, yielding the corresponding donor-spirobifluorene-acetylene compound as shown in Figure 5. The structures were confirmed by ^{1}H and ^{13}C NMR spectroscopy, with spectra provided in the Supporting Information (Figure S5 and S6).

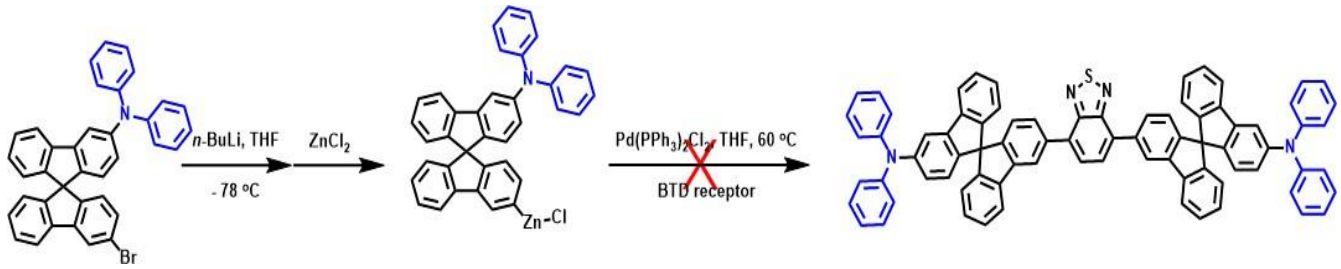

Figure 4. Synthesis of D-π-A luminescent materials (Negishi Coupling).

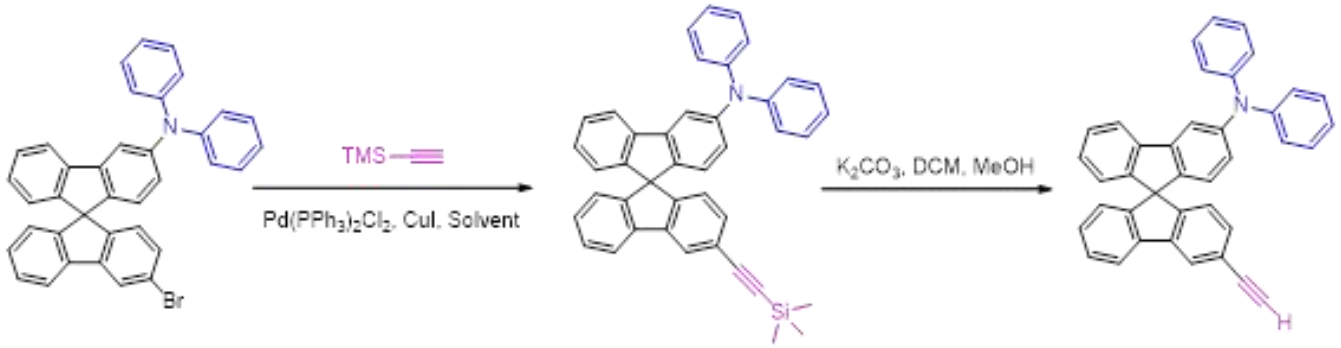

Figure 5. Sonogashira coupling and deprotection of TMS groups.

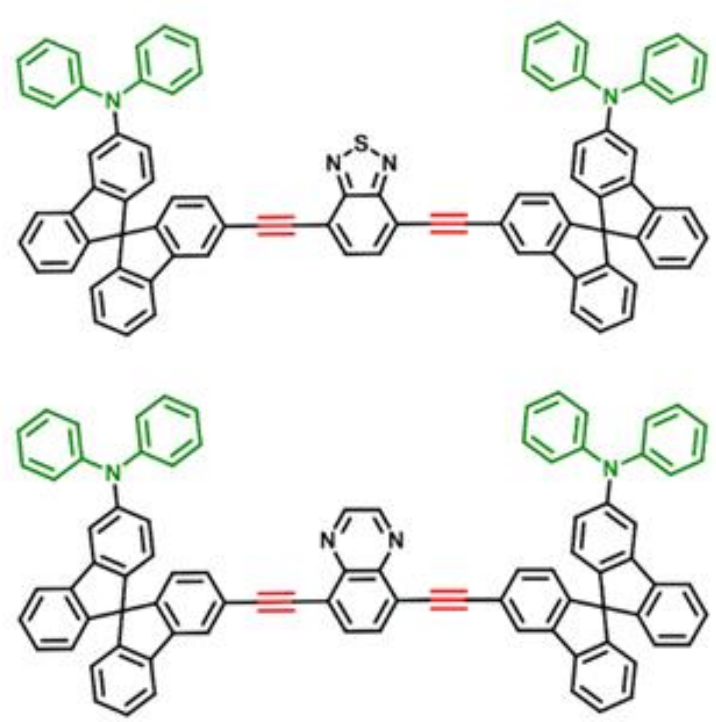

Figure 6. Synthesis of D-π-A luminescent materials (Sonogashira Coupling).

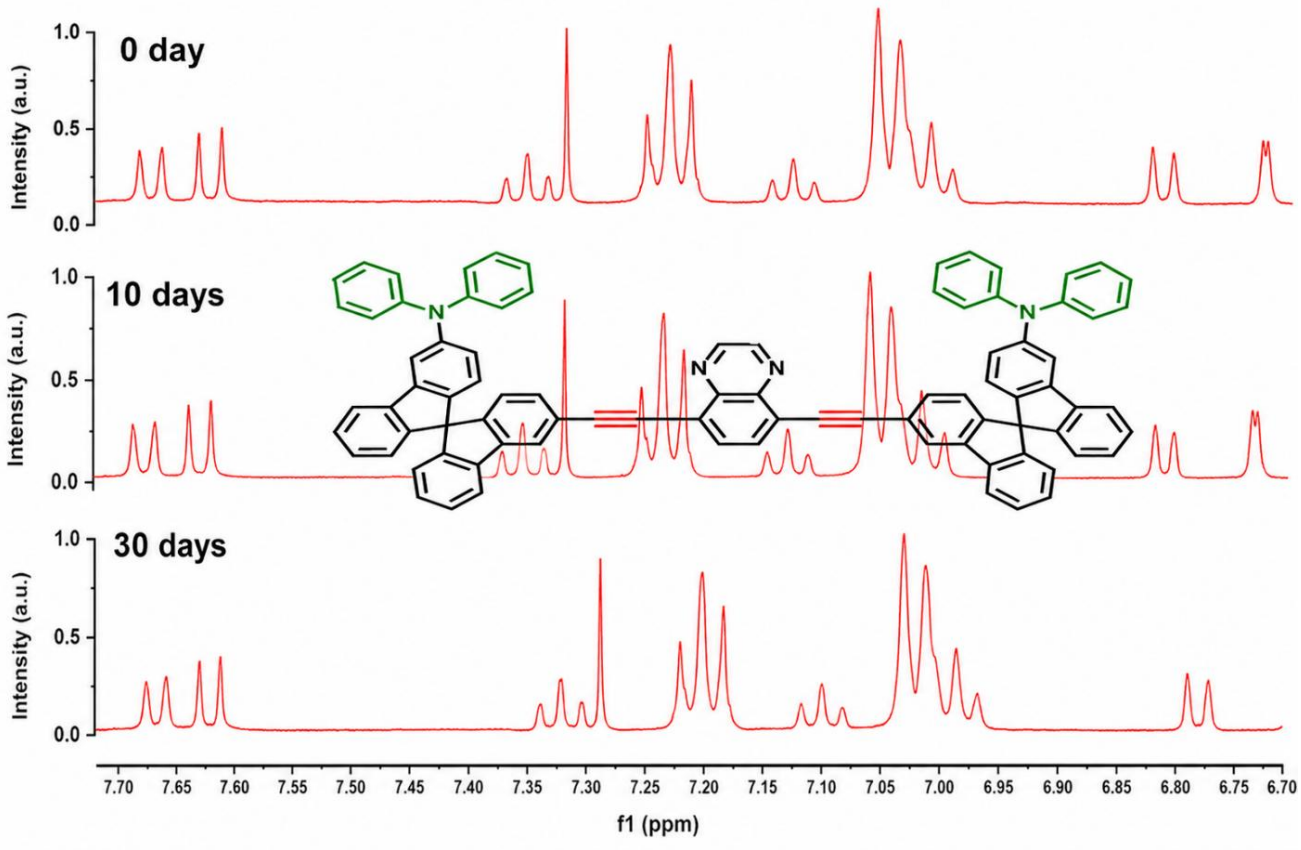

Figure 7. Comparison of ^{1}HNMR spectra of compound BTD-DPA in $CDCl_3$ stored under ambient conditions for different times.

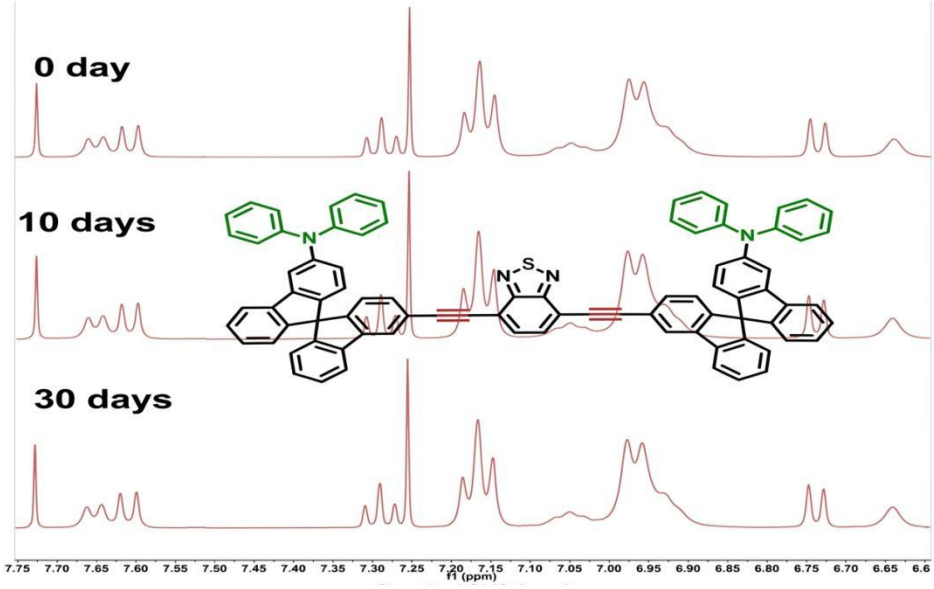

Figure 8. Comparison of 1HNMR spectra of compound QXN-DPA in CDCl3 stored under ambient conditions for different times.

3.2. Solution-state stability studies

After successfully preparing the D-π-A-π-D type luminescent materials BTD-DPA and QXN-DPA, their stability toward water and oxygen was investigated. Each compound was dissolved in deuterated chloroform and stored in ambient air at room temperature. The residual $CDCl_3$ signal at 7.26 ppm was used as an internal reference, as shown in Figure 7 and 8. The NMR results revealed no significant changes in signal peaks for either compound after the specified time periods. No additional resonances attributable to decomposition products were observed, and the relative integration of characteristic aromatic proton signals remained unchanged throughout the monitoring period [35]. These results indicate that both BTD-DPA and QXN-DPA possess good stability under aerobic and moist conditions in solution.

3.3. Study on the Photophysical Properties in Solution

The photophysical behavior of quinoxaline (QXN) and benzothiadiazole (BTD) derivatives was investigated by UV-Vis absorption and fluorescence spectroscopy in dichloromethane. As shown in Figure 9a-b, QXN displayed absorption bands at 314 nm and 355 nm, attributed to π-π* electronic transitions of the conjugated heteroaromatic framework. The corresponding fluorescence spectrum showed emission centered at 440-460 nm, consistent with intramolecular charge transfer character [34-36]. BTD exhibited broader absorption in the UV region with an onset near 370 nm (Figure 9c), arising from π-π* transitions within its electron-deficient core. The fluorescence spectrum of BTD (Figure 9d) showed an emission band between 400 and 450 nm with lower intensity compared to QXN under identical conditions. Both chromophores exhibited UV absorption, with QXN showing higher emission intensity in solution. The solvent-dependent optical properties of BTD-DPA and QXN-DPA were investigated by UV-Vis absorption and fluorescence spectroscopy. The absorption spectra of QXN-DPA (Figure 10a) revealed bands in the UV region that remained largely invariant across solvents of different polarity, indicating that ground-state electronic transitions are not strongly influenced by the medium. In contrast, the fluorescence spectra of QXN-DPA (Figure 10b) displayed observable solvatochromism, with the emission maximum shifting to longer wavelengths from nonpolar solvents (hexane, toluene) to more polar media (DCM, DMSO). This behavior is consistent with an intramolecular charge transfer state that is stabilized in polar environments. Similarly, BTD-DPA exhibited absorption features with negligible solvent dependence (Figure 10c) [39-43].

The fluorescence spectra of BTD-DPA (Figure 10d) showed solvent-dependent behavior, with changes in both emission intensity and wavelength across solvents. Higher emission intensities were observed in moderately polar solvents such as THF and toluene, suggesting that the emissive state of BTD-DPA is influenced by the balance between solvent polarity and nonradiative deactivation pathways. Collectively, these observations indicate that while the absorption profiles of the studied chromophores are relatively solvent-independent, their photoluminescence responses are modulated by solvent polarity, consistent with the stabilization of ICT states in polar media and differential quenching effects across solvents [44-47].

The photophysical properties of QXN-DPA and BTD-DPA were evaluated in toluene and are summarized in Table S5. QXN-DPA exhibited absorption at 310 nm and fluorescence emission centered around 450 nm, whereas BTD-DPA showed absorption near 352 nm with emission around 400 nm [48-53].

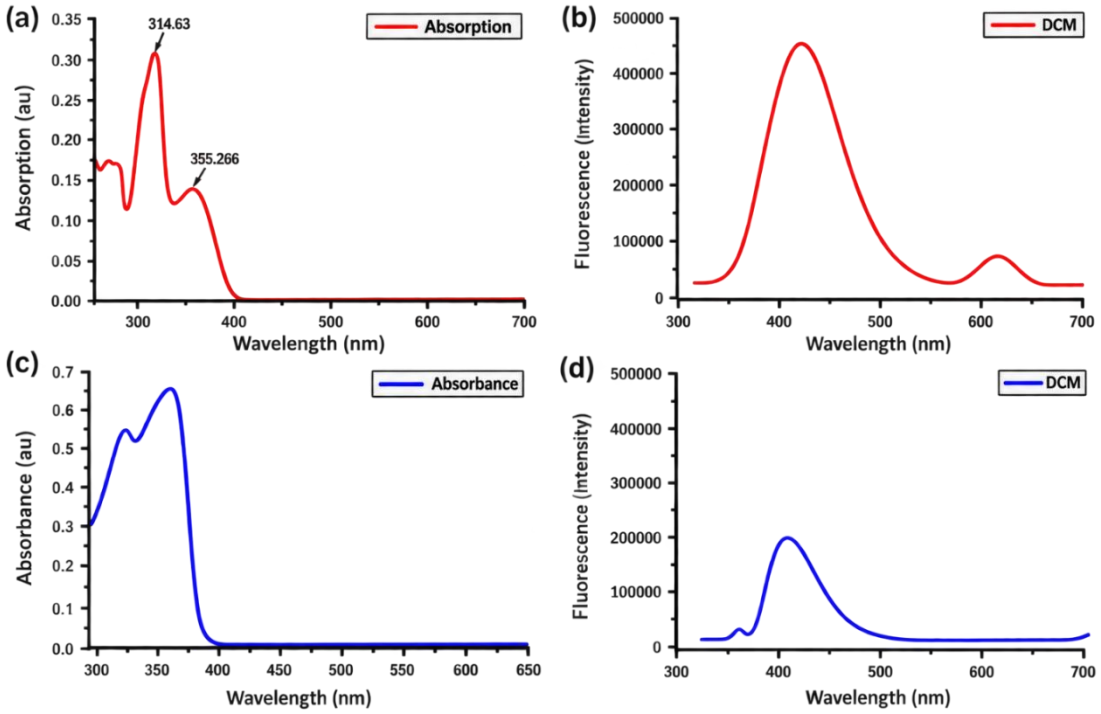

Figure 9. UV-Vis absorption spectra of D-π-A type organic boron luminescent molecule (dichloromethane solution); a) absorption spectra of QXN-DPA; b) fluorescence spectra of QXN-DPA; c) absorption spectra of BTD-DPA; d) fluorescence spectra of BTD-DPA.

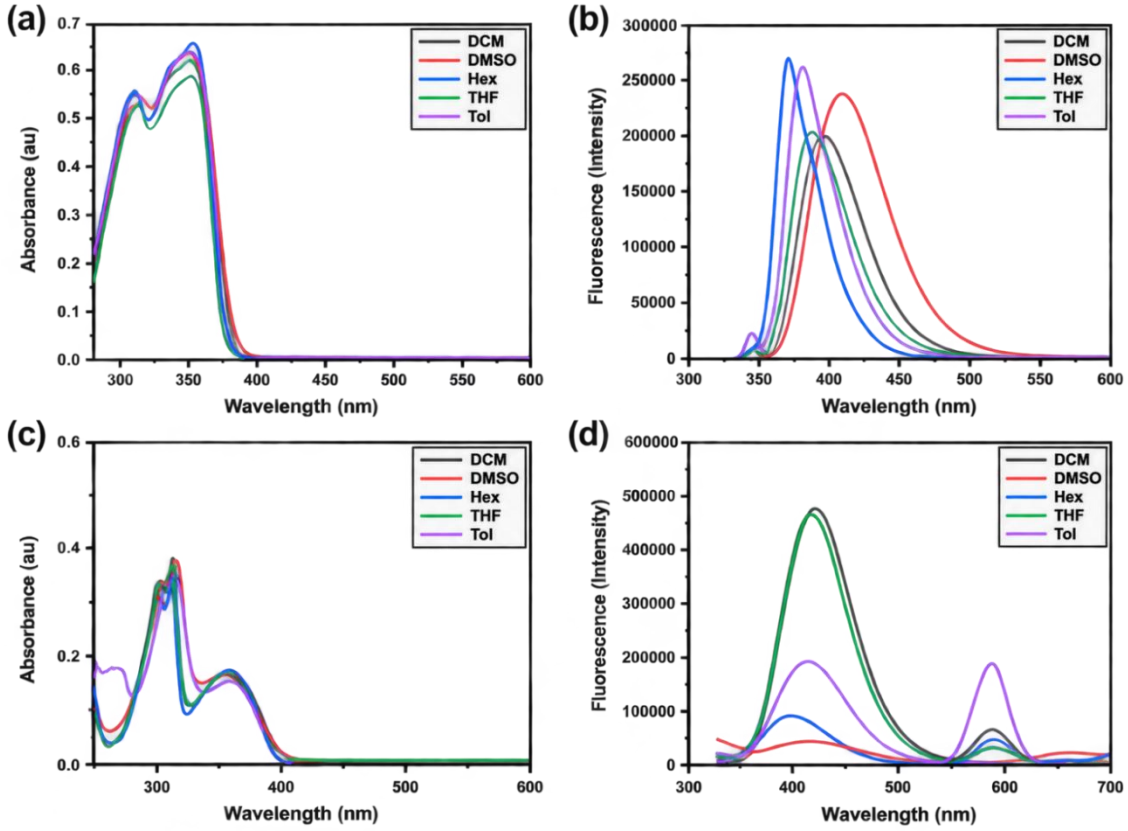

Figure 10. Comparison of UV-Vis absorption and fluorescence spectra in different solvents: a) UV-Vis absorption spectra of QXN-DPA; b) fluorescence spectra of QXN-DPA in different solvents; c) UV-Vis absorption spectra of BTD-DPA; d) fluorescence spectra of BTD-DPA in different solvents.

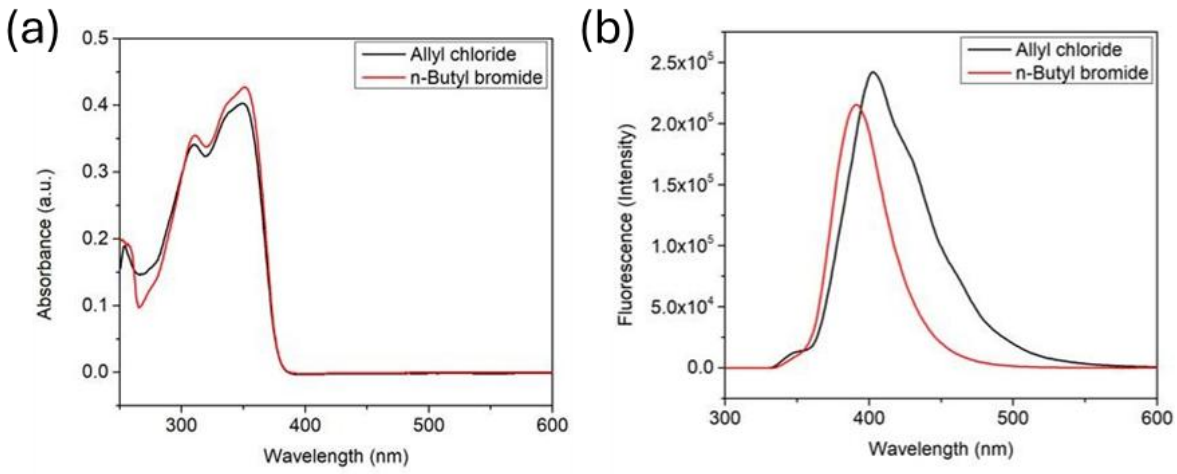

Figure 11. a) Comparison of UV-Vis absorption and b) emission spectra in Allyl chloride and n-Butyl bromide solutions.

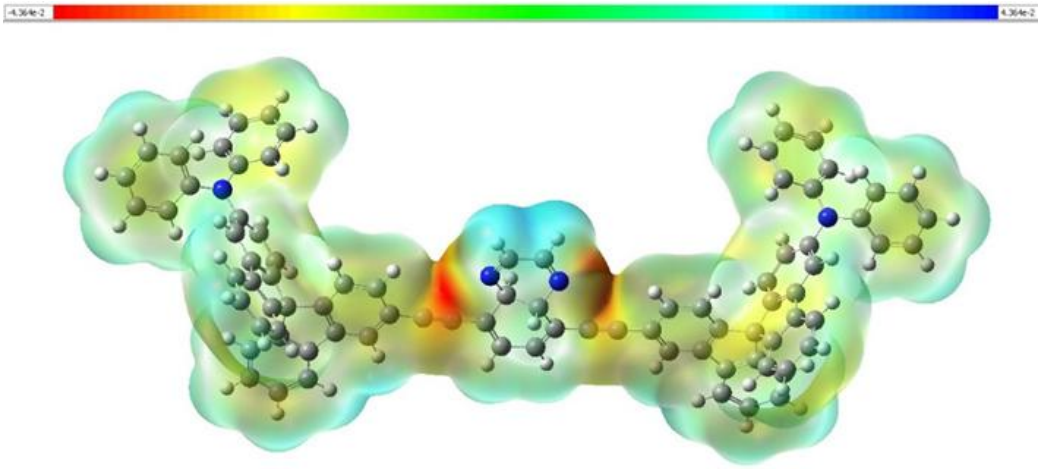

Figure 12. MEP surface mapped onto electron density, showing electron-rich (red) regions near N atoms and π-systems, and electron-deficient (blue) areas near H atoms.

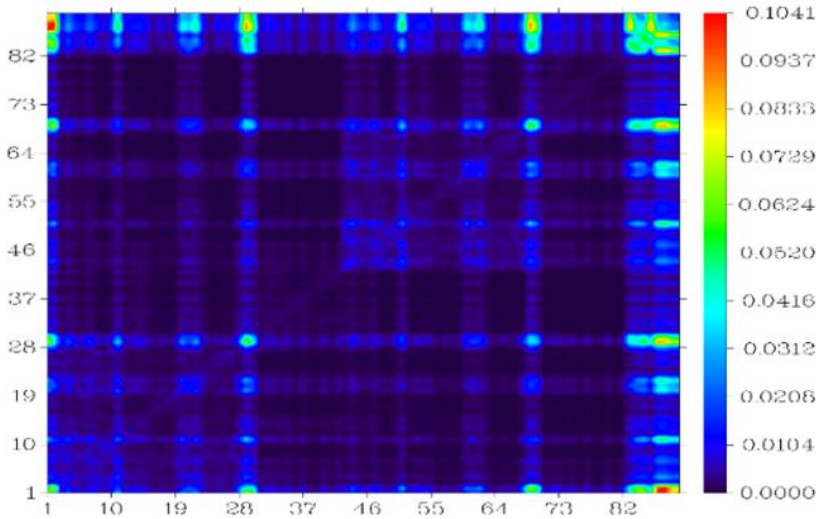

Figure 13. TDM plot showing localized π–π excitations and moderate charge-transfer, reflecting the molecule's conjugation and electronic structure.

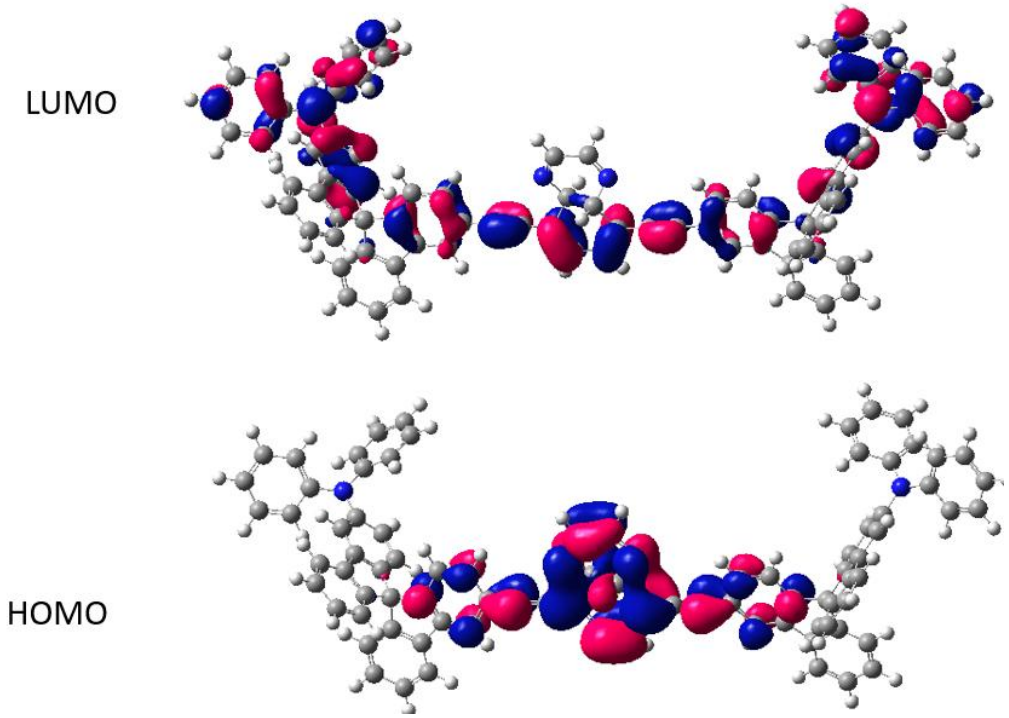

Figure 14. Frontier orbital analysis showing HOMO localized on the central π-core and LUMO delocalized across the conjugated bridge, indicating π→π excitation with partial charge-transfer character.

Both compounds displayed large Stokes shifts, consistent with excited-state relaxation involving intramolecular charge-transfer character. Fluorescence quantum yields of 14.3% for QXN-DPA and 16.4% for BTD-DPA were obtained under identical experimental conditions. A direct comparison showed that BTD-DPA exhibited a red-shifted absorption maximum at 352 nm compared with 310 nm for QXN-DPA. In contrast, QXN-DPA displayed longer-wavelength emission at approximately 450 nm and a larger apparent Stokes shift than BTD-DPA, which emitted near 400 nm. BTD-DPA also showed a slightly higher fluorescence quantum yield of 16.4%, compared with 14.3% for QXN-DPA. These differences demonstrate that the acceptor unit strongly influences the absorption energy, excited-state relaxation, emission wavelength, and fluorescence efficiency of the compounds. The optical band gaps estimated from the absorption onsets were approximately 2.43–2.44 eV for both compounds. Differences in absorption and emission behavior between the two systems reflect the influence of acceptor identity on the electronic structure and excited-state properties of the spirobifluorene-based D–π–A–π–D framework.

The fluorescence behavior of BTD-DPA was further examined in halogenated solvents with different heavy-atom characteristics, namely allyl chloride and n-butyl bromide (Figure 11). A reduction in fluorescence intensity was observed in the brominated solvent, which may arise from enhanced spin–orbit coupling associated with the external heavy-atom effect. These observations suggest possible changes in excited-state deactivation pathways; however, additional time-resolved spectroscopic measurements would be required to establish the precise mechanism [54-57]..

3.4. Computational studies

To obtain further molecular-level insight into the experimentally observed charge-transfer behavior, computational analysis was performed for QXN-DPA. Representative DFT calculations were performed on QXN-DPA to qualitatively examine the electronic distribution and charge-transfer characteristics of the designed molecular framework. Since both compounds possess identical donor and bridge units, the calculations provide general insight into the electronic behavior of the related BTD-DPA system. The molecular electrostatic potential (MEP) surface of **QXN-DPA** was calculated using DFT at the B3LYP/6-31G(d) level of theory and mapped onto the electron density surface to visualize charge distribution (Figure 12). The potential values ranged from -0.0436 a.u. (deep red regions) to +0.0436 a.u. (deep blue regions), indicating moderate molecular polarity. Red regions, primarily localized around nitrogen atoms and π-rich aromatic moieties, corresponded to areas of high electron density, suggesting potential sites for electrophilic attack and hydrogen bond acceptor capability [42]. Conversely, blue regions near hydrogen atoms and positively polarized areas represented electron-deficient sites, which could act as potential nucleophilic attack points or hydrogen bond donors. The predominance of green and yellow areas reflected relatively

neutral electrostatic regions, consistent with the molecule's conjugated aromatic framework.

Overall, the MEP analysis highlighted the localized charge distribution and supported the molecule's capacity for intermolecular interactions through hydrogen bonding and π-π stacking. The transition density matrix (TDM) of **QXN-DPA** was computed to analyze the nature of its low-energy electronic excitations. The TDM plot (Figure 13) maps the transition density contributions between occupied and virtual molecular orbitals, with the color scale ranging from 0.0000 (dark blue) to 0.1041 (red). The plot shows dominant contributions concentrated near the diagonal, indicating that the primary excitations are localized within specific conjugated fragments. However, several off-diagonal elements appear, reflecting charge-transfer character between different parts of the molecule. This dual nature of excitations—localized π-π* transitions complemented by charge-transfer interactions—suggests that the molecule's electronic structure is influenced by its extended π-conjugation and electron-rich heteroatoms. These features are consistent with the observed optical absorption properties and the solvatochromism observed in fluorescence studies.

Frontier orbital analysis of QXN-DPA showed that the HOMO is mainly localized on the central π-core and diphenylamine donor, whereas the LUMO is delocalized along the conjugated bridge and onto the quinoxaline acceptor (Figure 14). This distribution is consistent with a π→π* excitation that acquires partial charge-transfer character. From the orbital energy diagram, the HOMO and LUMO energies were calculated as -0.18890 a.u. (orbital 299) and -0.08787 a.u. (orbital 300), respectively, giving an energy gap of ΔE = 0.10103 a.u. = 2.75 eV (1 a.u. = 27.2114 eV). The corresponding optical onset wavelength was calculated as approximately 451 nm (λ ≈ 1240/ΔE), which aligns with the experimental absorption onset and the mixed localized/charge-transfer features observed in the TDM analysis. Isosurfaces of the HOMO and LUMO and the associated orbital energy diagram are shown in Figure 14.

4. Conclusion

In summary, two spirobifluorene-based D-π-A-π-D compounds incorporating benzothiadiazole and quinoxaline acceptor units were successfully synthesized through a Sonogashira coupling strategy that effectively addressed steric hindrance limitations encountered in conventional cross-coupling reactions. Both compounds exhibited good solution stability under ambient conditions, with no observable degradation detected by ^{1}H NMR spectroscopy after 30 days. Photophysical investigations revealed characteristic intramolecular charge-transfer behavior, including solvent-dependent fluorescence responses and acceptor-dependent absorption and emission properties. Comparative analysis demonstrated that the identity of the acceptor unit significantly influences the optical behavior and fluorescence efficiency of the molecular system. Computational analysis further supported the mixed localized and charge-transfer nature of the excited states. Overall, this work provides insight into structure-property relationships in sterically hindered spirobifluorene-based donor-acceptor luminophores and demonstrates an effective synthetic approach for constructing such architectures through alkyne-linked coupling strategies. Further investigations involving solid-state photophysical characterization and device studies will be necessary to evaluate their broader applicability in luminescent material systems.

Author contributions

Maria Siddique, as the primary author, led conceptualization, manuscript drafting, figure creation, and revisions. Rafaqat Khan, Zeeshan Akmal, Amir Zeeshan and Muhammad Mubashir Khan organized the figure design and manuscript refinement for clarity and technical accuracy. Mazhar Khan, Qifan Yan, supervised the project, provided critical revisions, and finalized the manuscript. All authors have read and approved the final version.

Ethical approval

Not applicable.

Conflicts of Interest

The authors report no conflicts of interest.

Acknowledgment

Authors are thankful to the School of Chemistry and Molecular Engineering, East China University of Science & Technology, Shanghai 200237, P. R. China for the support.

Data availability statement

All the data used here are mentioned either in the manuscript or in the supplementary information.

Supplementary material

The Supplementary Material for this article can be found online at:
https://www.jspae.com/index.php/jce/article/view/948/398

Funding

Not Applicable (N/A).

REFERENCES

1. Cinar, M.E., et al., Thieno[2,3-b]thiophene based polymers: Synthesis and optoelectronic properties. European Polymer Journal, 2018. 104: p. 72-80.
2. Yamaguchi, S., et al., Dibenzoborole-containing π-electron systems: Remarkable fluorescence change based on the "on/off" control of the pπ–π* conjugation. Journal of the American Chemical Society, 2002. 124(30): p. 8816-8817.
3. Alam, M., et al., Development of a robust procedure for the copper-catalyzed ring-opening of epoxides with Grignard reagents. Organic Process Research & Development, 2012. 16(3): p. 435-441.
4. Wakamiya, A., et al., A B–B bond-containing polycyclic π-electron system: Dithieno-1,2-dihydro-1,2-diborin and its

dianion. Journal of the American Chemical Society, 2009. 131(31): p. 10850-10851.
5. Katayama, T., et al., Two-step synthesis of boron-fused double helicenes. Journal of the American Chemical Society, 2016. 138(16): p. 5210-5213.
6. Chen, D.M., et al., Synthesis and properties of B,N-bridged p-terphenyls. Chemical Communications, 2014. 50: p. 782-784.
7. Noda, H., et al., Unique physicochemical and catalytic properties dictated by the B3NO2 ring system. Nature Chemistry, 2017. 9: p. 571-577.
8. Krieg, M., et al., Construction of an internally B3N3-doped nanographene molecule. Angewandte Chemie International Edition, 2015. 54: p. 8284-8286.
9. Sheng, W., et al., Synthesis, characterization, and tunable semiconducting properties of aza-BODIPY derived polycyclic aromatic dyes. Science China Chemistry, 2020. 63(9): p. 1240-1245.
10. Wang, X.Y., et al., Synthesis of stable nanographenes with OBO-doped zigzag edges based on tandem demethylation-electrophilic borylation. Journal of the American Chemical Society, 2016. 138(29): p. 9021-9024.
11. Biswas, S., et al., Synthesis and structural characterization of 9-azido-9-borafluorene: Monomer and cyclotrimer of a borole azide. Inorganic Chemistry, 2010. 49(10): p. 4499-4506.
12. Zhuang, F.D., et al., BN-embedded tetrabenzopentacene: A pentacene derivative with improved stability. Angewandte Chemie International Edition, 2019. 58(31): p. 10708-10712.
13. Wang, X., et al., Concise approach to T-shaped NBN-phenalene cored luminogens as intensive blue light emitters. Chemistry - A European Journal, 2020. 26: p. 13966-13972.
14. Crumbach, M., et al., Dithiophene-fused oxadiborepins and azadiborepins: A new class of highly fluorescent heteroaromatics. Angewandte Chemie, 2021. 133(17): p. 9376-9381.
15. Franceschini, M., et al., Peri-acenoacene ribbons with zigzag BN-doped peripheries. Journal of the American Chemical Society, 2022. 144(47): p. 21470-21484.
16. Bontemps, S., et al., Phosphino-boryl-naphthalenes: Geometrically enforced, yet Lewis acid responsive P→B interactions. Inorganic Chemistry, 2013. 52(8): p. 4714-4720.
17. Numano, M., et al., Synthesis of boronate-based benzo[fg]tetracene and benzo[hi]hexacene via demethylative direct borylation. Chemistry - A European Journal, 2016. 22(33): p. 11574-11577.
18. Hertz, V.M., et al., Boron-containing polycyclic aromatic hydrocarbons: Facile synthesis of stable, redox-active luminophores. Angewandte Chemie, 2015. 127: p. 8924-8928.
19. Smith, M.F., et al., Substituent effects on the properties of borafluorenes. Organometallics, 2016. 35(18): p. 3182-3191.
20. Crossley, D.L., et al., A modular route to boron doped PAHs by combining borylative cyclisation and electrophilic C-H borylation. Chemical Science, 2017. 8(12): p. 7969-7977.
21. Yan, Q., et al., An air-stable organoboron compound, dithienooxadiborepine: Preparation and functionalization. Journal of Organic Chemistry, 2018. 83(16): p. 9096-9102.
22. Zhang, J.J., et al., One-pot synthesis of boron-doped polycyclic aromatic hydrocarbons via 1,4-boron migration. Angewandte Chemie International Edition, 2021. 60(6): p. 2833-2838.
23. Xia, Y., et al., 6,12-Dihydro-6,12-diboradibenzo[def,mno]chrysene: A doubly boron-doped polycyclic aromatic hydrocarbon for organic light emitting diodes by a one-pot synthesis. Organic Letters, 2020. 22(20): p. 7942-7946.
24. Zi, L., et al., Synthesis, properties, and reactivity of bis-BN phenanthrenes: Stepwise bromination of the main scaffold. Organic Letters, 2020. 22(4): p. 1499-1503.
25. Sun, Z., et al., π-Extended C2-symmetric double NBN-heterohelicenes with exceptional luminescent properties. Organic Letters, 2020. 22(1): p. 209-213.
26. Dosso, J., et al., Synthesis and optoelectronic properties of hexa-peri-hexabenzoborazinocoronene. Angewandte Chemie, 2017. 129(16): p. 4554-4558.
27. Guo, Y., et al., BN/BO-ullazines and bis-BO-ullazines: Effect of BO doping on aromaticity and optoelectronic properties. Journal of Organic Chemistry, 2021. 86(18): p. 12507-12516.
28. Gu, Y., et al., Peri-acenoacene for solution processed distributed feedback laser: The effect of 1,2-oxaborine doping. Advanced Optical Materials, 2022. 10(7): p. 2102782.
29. Dong, X., et al., Synthesis, crystal structure, aggregation-induced emission enhancement and electroluminescence properties of a novel compound containing carbazole and triarylborane groups. Journal of Molecular Structure, 2021. 1228: p. 129721.
30. Maggiore, A., et al., Novel easy to synthesize benzonitrile compounds with mixed carbazole and phenoxazine substituents exhibiting dual emission and TADF properties. Journal of Physical Chemistry B, 2022. 126(14): p. 2740-2753.
31. Zhang, Y., et al., Pyrrolic type N directed borylation route to BN-PAHs: Tuning the photophysical properties by varying the conjugation shape and size. Journal of Organic Chemistry, 2021. 86(9): p. 6322-6330.
32. Campbell, P.G., et al., Recent advances in azaborine chemistry. Angewandte Chemie International Edition, 2012. 51: p. 6074-6092.
33. Ashe, A.J., et al., A synthesis of aromatic five- and six-membered B-N heterocycles via ring closing metathesis. Organic Letters, 2000. 2(14): p. 2089-2091.
34. Marwitz, A.J., et al., Diversity through isosterism: The case of boron-substituted 1,2-dihydro-1,2-azaborines. Organic Letters, 2007. 9(23): p. 4905-4908.
35. Agou, T., et al., Syntheses, structure, and optical properties of ladder-type fused azaborines. Organic Letters, 2006. 8(11): p. 2241-2244.
36. Hatakeyama, T., et al., Synthesis of BN-fused polycyclic aromatics via tandem intramolecular electrophilic arene borylation. Journal of the American Chemical Society, 2011. 133(46): p. 18614-18617.
37. Ma, M., et al., Rational utilization of intramolecular hydrogen bonds to achieve blue TADF with EQEs of nearly 30% and single emissive layer all-TADF WOLED. ACS Applied Materials & Interfaces, 2021. 13(37): p. 44615-44627.
38. Zhou, Y., et al., White light luminescence from a homo-conjugated molecule with thermally activated delayed fluorescence. Chemistry - An Asian Journal, 2021. 16(14): p. 1893-1896.
39. Saragi, T.P., et al., Spiro compounds for organic optoelectronics. Chemical Reviews, 2007. 107(4): p. 1011-1065.
40. Sun, C.J., et al., BN-functionalized benzotrithiophene-based azaborines: Synthesis, structures, and anion binding properties. Inorganic Chemistry, 2019. 58(6): p. 3591-3595.
41. Min, Y., et al., Quadruply B←N-fused dibenzo-azaacene with high electron affinity and high electron mobility. Journal of the American Chemical Society, 2019. 141(42): p. 17015-17021.
42. Okada, N., et al., Synthesis and late-stage diversification of BN-embedded dibenzocorannulenes as efficient fluorescence organic light-emitting diode emitters. Chemistry - A European Journal, 2023. 29(5): p. e202202627.

43. Zhang, Y., et al., Synthetic doping of acenaphthylene through BN/CC isosterism and a direct comparison with BN-acenaphthene. Journal of Organic Chemistry, 2022. 87(19): p. 12986-12996.
44. Ju, C.W., et al., Modular synthesis of pentagonal and hexagonal ring-fused NBN-phenalenes leading to an excited-state aromatization-induced structural planarization molecular library. Journal of the American Chemical Society, 2021. 143(15): p. 5903-5916.
45. Li, M., et al., Engineering spatially adjacent redox sites with synergistic spin polarization effect to boost photocatalytic CO2 methanation. Journal of the American Chemical Society, 2024. 146(22): p. 15538-15548.
46. Khan, M., et al., MOFs materials as photocatalysts for CO2 reduction: Progress, challenges and perspectives. Carbon Capture Science & Technology, 2024. 11: p. 100191.
47. Tayyab, M., et al., Visible light-driven photocatalytic H2 evolution and dye degradation by electrostatic self-assembly of CdS nanowires on Nb2C MXene. International Journal of Hydrogen Energy, 2024. 51: p. 1400-1413.
48. Tayyab, M., et al., A binary dumbbell visible light driven photocatalyst for simultaneous hydrogen production with the selective oxidation of benzyl alcohol to benzaldehyde. Journal of Colloid and Interface Science, 2024. 665: p. 911-921.
49. Mansoor, S., et al., Recent advancements in Se and Te-enriched cocatalysts for boosting photocatalytic splitting of water to produce hydrogen. Research on Chemical Intermediates, 2023. 49(9): p. 3723-3745.
50. Ahmad, M.N., et al., Photocatalytic degradation of Yellow-50 using ZnO/polyorthoethylaniline nanocomposites. JOM, 2022. 74(5): p. 2106-2112.
51. Mansoor, S., et al., Novel RuSe2/Ti3C2 nanosheets incorporating into ZnIn2S4 nanoflowers with S-scheme charge transfer for photocatalytic hydrogen evolution. Journal of Colloid and Interface Science, 2025. 699: p. 138217.
52. Khan, M., et al., Engineering spatially proximate redox sites in Pd-In/TiO2 photocatalyst for selective CO2 photoreduction. Applied Surface Science, 2025. 709: p. 163644.
53. Khan, M., et al., Integration of CO2 activation and photogenerated electron accumulation at Ti site via dual tandem electric fields in BiOBr MIL 125 heterojunction for boosting CO2 photoreduction. Applied Catalysis B: Environment and Energy, 2025. 370: p. 125165.
54. Mansoor, S., et al., Simultaneous hydrogen production with photo reforming of lactic acid over MXene derived MoS2/TiO2/Ti3C2 nanowires. Chinese Journal of Catalysis, 2025. 71: p. 234-245.
55. Wang, L., et al., High loading Cu single atom engineering on g-C3N4 for visible light CO2 photoreduction. Small, 2025. 21(27): p. 2503390.
56. Khan, M., et al., Engineering NH2-MIL-125(Ti)@ZnIn2S4 S-scheme heterostructure for boosting CO2 photoreduction. Separation and Purification Technology, 2025. 379: p. 134819.
57. Khan, M., et al., Core shell MIL-125(Ti)@In2S3 S-scheme heterojunction for boosting CO2 photoreduction. ACS Applied Materials & Interfaces, 2025. 17(21): p. 30895-30909.

How to cite this article:
Siddique, M., Khan, M., Khan, M. M., Zeeshan, A., Akmal, Z., Khan, R., & Yan, Q. Alkyne-Linked Spirobifluorene D–π–A–π–D Emitters: Synthesis, Solution-State ICT Photophysics, and Comparative Acceptor Effects. Journal of Chemistry and Environment, 5(2), 17–28.